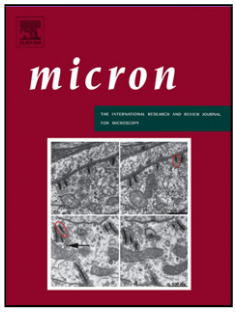

Title: New Approach to Electron Microscopy Imaging of Gel Nanocomposites *in situ*

Authors: Alejandra Londono-Calderon, Srikanth Nayak, Curtis L. Mosher, Surya K. Mallapragada, Tanya Prozorov

PII: S0968-4328(18)30476-1
DOI: https://doi.org/10.1016/j.micron.2019.02.010
Reference: JMIC 2663

To appear in: *Micron*

Received date: 15 December 2018
Revised date: 20 February 2019
Accepted date: 20 February 2019

Please cite this article as: Londono-Calderon A, Nayak S, Mosher CL, Mallapragada SK, Prozorov T, New Approach to Electron Microscopy Imaging of Gel Nanocomposites *in situ*, *Micron* (2019), https://doi.org/10.1016/j.micron.2019.02.010

New Approach to Electron Microscopy Imaging of Gel Nanocomposites *in situ*

Alejandra Londono-Calderon[1], Srikanth Nayak[1,2], Curtis L. Mosher[3], Surya K. Mallapragada[1,2], and Tanya Prozorov[1*]

[1]Division of Materials Science and Engineering, US DOE Ames Laboratory, Ames, IA, 50011
[2]Department of Chemical and Biological Engineering, Iowa State University, Ames, IA, 50011
[3]Roy J. Carver High Resolution Microscopy Facility, Iowa State University, Ames, IA, 50011

[*]Corresponding Author: tprozoro@ameslab.gov

Highlights

- Fluid cell S/TEM is suitable for characterization of gel-based nanocomposites
- Controlled deposition of femtoliter-range viscous specimen onto SiN windows is shown
- Nanoparticles as small as 5 nm, dispersed in 600 nm thick gel layer are resolved
- No visible signs of electron beam damage are observed under experimental conditions
- New approach is free of artifacts associated with conventional sample preparation

Abstract

Characterization of Au-nanocomposites is routinely done with scattering techniques where the structure and ordering of nanoparticles can be analyzed. Imaging of Poloxamer gel-based Au-nanocomposites is usually limited to cryo-TEM imaging of cryo-microtomed thin sections of the specimen. While this approach is applicable for imaging of the individual nanoparticles and gauging their size distribution, it requires altering the state of the specimen and is prone to artifacts associated with preparation protocols. Use of Scanning Transmission Electron Microscopy (S/TEM) with fluid cell *in situ* provides an opportunity to analysis of these complex materials in their hydrated state with nanometer

resolution, yet dispensing dense gel-based samples onto electron-transparent substrates remains challenging. We show that Poloxamer gel-based Au nanocomposites exhibiting thermoreversible behavior can be imaged in a fully hydrated state using a commercially available fluid cell holder, and we describe a specimen preparation method for depositing femtoliter amounts of gel-based nanocomposites directly onto the 50 nm-thick SiN window membranes. Ultimately, fluid cell S/TEM *in situ* imaging approach offers a pathway to visualization of individual nanoparticles within a thick gel media while maintaining hydrated state of the carrier polymeric matrix.

Keywords: fluid cell S/TEM, gel-based nanocomposite, nanoparticle imaging, signal-to-noise ratio

1. Introduction

Self-assembly of block copolymers into microphase separated domains has been utilized for the templated synthesis and assembly of mesoporous materials [1-3] and nanocomposites [3-7]. These nanocomposites have many potential applications in a number of important fields, such as optical materials[5,8], biomedicine[9,10], nonvolatile memory devices[11,12], among other [13,14]. Use of block copolymers offers a pathway for a targeted formation and placement of nanoparticles with controlled ordering of spatial arrangement within the matrices of these materials. Interactions between the individual blocks of the polymer with Au nanoparticles can lead to enhanced nanoparticle stability and biocompatibility. A family of block copolymers with polyethylene oxide (PEO) and polypropylene oxide (PPO) blocks, form amphiphilic chains with modulated thermoresponsive properties corresponding to the block units, length of chain and relative molecular weight. Triblock copolymers with the PEO-PPO-PEO chain architecture are commonly known as Poloxamers, and show micellization behavior in water. Above a critical temperature and concentration, these block copolymer solutions undergo a reversible liquid-to-gel transition and form a physical hydrogel. Although the mechanism of formation and self-assembly of thermoresponsive gels are not completely understood, they have been used as templates for the assembly of nanoparticle arrays [15-20], for biomimetic nanocomposite synthesis [21-23], and mesoporous materials [24-26]. Gyroid and lamellar phases shown by Poloxamers are of particular interest in obtaining templated assemblies of metallic nanoparticles for optical properties [27,28]. Theoretical simulations suggest the formation of polymer-templated composite phases with unusual morphologies based on triblock copolymers, such as Poloxamers [29-31].

Structural characterization of aqueous Poloxamer gels is normally addressed by using Small Angle Scattering techniques (SAXS or SANS). Due to complex solubility of these copolymers in water, aqueous Poloxamer gels exhibit reverse thermoresponsive behavior, and their handling limits direct

imaging of the polymeric assembly to bright field cryo-TEM of thin sections of either freeze-dried or vitrified samples [32-35]. This approach has been extended to characterization of nanoparticles in gel media [36,37] to include viewing of the individual nanoparticles captured within thin sections of the gels and gauging their size distribution. The majority of studies involving biological materials using TEM are routinely carried out in the absence of a liquid environment, and the high vacuum of the electron microscope makes the imaging of such specimens in their native, unaltered state, impossible. While cryo-TEM imaging yields snapshots of nanoparticle distributions within the thin slices of prepared specimens, the technique is notorious for dealing with artifacts associated with the specimen preparation protocols ranging from vitreous ice contamination to temperature gradients, to inhomogeneous vitrification and uneven specimen thickness, to movement and loss of nanoparticles during the cryomicrotoming process. When imaging dispersed nanoparticles, each of these artifacts can greatly affect the results.

The recent advances in fluid cell TEM specimen holder technology provide new opportunities for the *in situ* characterization of various types of specimens in liquid phase with nanometer spatial resolution, as evidenced by numerous reports on inorganic nanoparticles [38,39], macromolecules [40], unlabeled proteins [41], eukaryotic cells [42] and bacteria [43]. Using this approach, a sample is sandwiched between two thin electron-transparent SiN window membranes, sealed to protect the liquid from the high vacuum environment and imaged using the scanning/transmission electron microscope. Imaging cryo-plunged and cryomicrotomed nanocomposites with BF-TEM cryomicroscopy reveals lateral distribution of nanoparticles physically constrained within a thin slice of a vitrified specimen. In the case of imaging of such viscous gel-like nanocomposite *in situ* with the fluid cell, the imaging would allow focusing nanoparticles located at the same depth in the latter. In both cases, the information acquired during the imaging, will be equivalent to obtaining a series of two-dimensional projections of a non-rigid three-dimensional spatial arrangement of nanoparticles. While obtaining of 3D structure of individual nanoparticles in liquid has been reported, analysis of spatial distribution of nanoparticles in liquid or gel matrix [44-46] would require optimization and commercialization of a new generation of fluid cell TEM holders. Until then, sample preparation protocols and imaging of hydrated viscous nanocomposite specimens, soft matter and biological specimens with nanoscale resolution with the fluid cell *in situ* in an unaltered state, can provide an alternative pathway to cryo-TEM [47]. Recently, Parent *et al*.[48,49] reported on use of fluid cell to analyze the growth of nanoparticles in block polymer and liquid crystal templates, showing remarkable achievements in the area of small nanoparticles undergoing *in situ* dynamic processes in dense solvents. Accurate dispensing of micro-volumes of viscous substances onto thin electron-transparent membranes with commonly available laboratory equipment is highly challenging.

Moreover, temperature-dependent viscosity of Poloxamer-based nanocomposites leading to gel formation and loss of flow in this materials at room temperature, further complicate the deposition process.

Here, we present a new approach suitable for direct visualization of nanoparticles dispersed in viscous media as a complementary or alternative to the bright field cryo-TEM imaging. We describe a novel approach to characterization of Poloxamer gel-based Au-nanocomposites as a model system with the fluid cell scanning/transmission electron microscope (FC-S/TEM) *in situ*, using aqueous F127 Poloxamer solutions containing dispersed Au nanoparticles, at polymer concentration of 22.7 wt%, known to form gels at room temperature. Two systems are described: F127 Poloxamer gel loaded with commercially available (ready) ~5nm Au nanoparticles, and citrate-bearing F127 Poloxamer gel containing ~13nm Au nanoparticles formed *in situ* (prepared) by reduction of $HAuCl_4$. We utilized a molecular printer to pattern the SiN window membranes with targeted amounts of Poloxamer-Au gel-based nanocomposites at controlled temperatures and under controlled humidity, followed by the S/TEM imaging of gel samples with a commercially available fluid cell holder, providing compatibility with the high vacuum environment of the electron microscope. The method described here offers a pathway to direct visualization and analysis of gel-based nanocomposites and characterization of individual nanoparticles dispersed in polymeric matrices.

2. Materials and Methods

2.1. Materials. Gold nanoparticles referred as ready nanoparticles, nominal diameter of 5 nm were purchased from Ted Pella Inc., Redding, CA. Poly(ethylene glycol)methyl ether thiol (m-PEG-SH) was purchased from Creative PEGWorks Inc., Mn ~ 5kDa. F127 Poloxamer, trisodium citrate dehydrate, and chloroauric acid tetrahydrate ($HAuCl_4 \cdot 4\ H_2O$) were purchased from Sigma Aldrich and used as received. Si_3N_4 window membranes (50 nm, 50 µm, 200 µm) were purchased from Hummingbird Scientific and plasma cleaned with UV/Ozone ProCleaner™ (Bioforce Nanosciences, Ames, IA, USA).

2.2. UV/vis absorbance spectra. UV/Vis absorbance spectra were acquired using Spectramax M3 spectrometer (Molecular Devices). For UV/Vis characterization a sample was taken from the concentrated suspension and diluted in water. Nanoparticle concentration was estimated using an absorbance value at 520 nm in the UV/Vis absorbance spectra ($\varepsilon = 5.4 \times 10^6\ M^{-1}\ cm^{-1}$).

2.3. Dynamic Light Scattering. Hydrodynamic radius of nanoparticles was determined by using a dynamic light scattering Zetasizer Nano-ZS90 (Malvern), HeNe laser, 633nm, 90º scattering angle.

2.4. Rheological measurements. Rheological measurements of the gelation behavior were conducted using an ARES G2 Rheometer (TA Instruments, New Castle, DE, USA.) equipped with Advanced Peltier

System for temperature control. Recessed concentric cylinders geometry was used (bob diameter: 27.66 mm, bob length 41.5 mm, cup diameter: 30 mm, operating gap: 5 mm, bob material: stainless steel). Temperature was ramped at a rate of 0.4 ºC/min. An oscillatory sinusoidal strain with 10% amplitude was applied at an angular frequency of 10 rad/s. Data sampling rate was set to 1 point/s.

2.5. Nanocomposite gel preparation. Gold nanoparticles (ready nanoparticles) were mixed with aqueous suspension of mPEG-SH at an excess for 2 days. Excess mPEG-SH was removed by dialysis with 20 kDa MWCO membrane against water for two days. The nanoparticles were then concentrated by evaporation of water at 37 ºC to obtain ~ 570 or 207 nM of gold nanoparticles. To a measured weight of this suspension, F127 Poloxamer powder was added to obtain solutions with the concentrations of 22.6 ± 0.05 wt% and 30 ± 0.05 wt%, respectively. For *in situ* preparation of gold nanoparticles in the polymer gels, F127 Poloxamer 4.5 mL of 25 wt% F127 in 20 mM Trisodium citrate was mixed and kept at ~ 4 ºC. The citrate gel was transferred to a pre-cooled 20 mL vial and mixed with 0.5 mL of 16 mM $HAuCl_4$ for a final concentration of 22.7 ± 0.05 wt% F127 in 18 mM Trisodium citrate and 1.6 mM $HAuCl_4$. The mixture was vortexed for 5 seconds and then kept at room temperature for 24 hours. For imaging of functionalized nanoparticles, ~ 3 μL of Au-PEG solution were deposited on a glow-discharged C-Cu grid and left to dry under ambient conditions. For imaging of citrate-Au nanoparticles prepared *in situ* in F127 Poloxamer, a small volume of gel nanocomposite was washed with copious amounts of cold water to remove polymeric matrix, after which ~3 μL of the resultant Au-citrate solution was deposited on a glow-discharged C-Cu grid and left to dry under ambient conditions. Both types of Au nanoparticles were imaged using FEI Tecnai G^2 F20 S/TEM operating at 200 kV, working in a bright field TEM mode.

2.6. Gel deposition and patterning conditions. Surface patterning of the SiN window membranes was carried out using a Nano eNabler™ molecular printing system (Bioforce Nanosciences, Ames, IA, USA) equipped with a custom-built temperature-controlled stage. Surface Patterning Tools (SPT) 10S or 30S (10 or 30 microns wide cantilever arm) were oxidized with a UV/Ozone ProCleaner™ for 40 minutes before use. The SiN window chips were used about an hour after plasma cleaning to decrease hydrophilicity. A small volume (~1 μL) of gel specimen was deposited on a cover slide with a micropipette tip to create a sample loading reservoir droplet, with the relative humidity in the chamber maintained at 52% to prevent drying of the polymer solution. The cover slide with the gel droplet and the deposition target SiN window chips were both loaded on the temperature-controlled stage set at the highest temperature below a gelation point at which the system was known to remain in a liquid state ($T<T_{gel}$). To mitigate condensation at the surface of SiN window membrane, we utilized an intermediate insulating thermal stage. A front-loading method was used to permit transfer of small amount of polymeric solution on SPT cantilever by gently immersing the cantilever into the sample loading

reservoir. Next, the polymer-loaded SPT was moved toward the target SiN window membrane for patterning the latter with polymer solution. The loaded SPT was positioned above a target SiN window. The SPT was repeatedly lowered to be brought into a contact with the target SiN window to deposit polymer solution at designated positions at the SiN window. The volume of polymer solution transferred to the SiN window, in general, depends on the viscosity of the sample, the humidity of the chamber, the size of the SPT, the wettability of the substrate, and contact time (the latter affects the volume of deposited droplet *via* its diameter), although this relationship is not calibrated. For the case of Au-Poloxamer nanocomposite specimens used in this work, the conditions presented here were found to be the most favorable for patterning of micro-droplets of similar sizes on SiN windows. For S/TEM imaging presented in this work, micro-droplets were obtaining by using a SPT 30S. The freshly patterned window chips were kept in a moist atmosphere until cell assembly. Images and video of a window patterning process were captured with the instrument NanoWare CB™ v1.3 software during the specimen deposition process.

2.7. 3D windows surface profiling. The surface profiling of the patterned windows was carried out using a Sensofar S neox Non-contact 3D Surface Profiler (Sensofar Metrology, Barcelona, Spain) equipped with a ferroelectric liquid crystal on silicon (FLCoS) microdisplay enabling a fast and stable scanning of confocal images with additional interferometry and focus variation scanning options. Patterned substrates were kept in moist atmosphere and imaged using a Nikon CF Plan Apo 150X/0.95 epi objective with a 0.1 micron vertical step size.

2.8. Fluid cell assembly and S/TEM characterization. The S/TEM images were recorded using FEI Tecnai G^2 F20 S/TEM equipped with a Tridium Gatan image filter operating at 200 kV in high angle annular dark field (HAADF) S/TEM mode. The *in situ* fluid cell S/TEM (FC-S/TEM) imaging was carried out using a commercial continuous flow fluid cell holder platform (Hummingbird Scientific, Lacey, WA, USA), with a removable tip designed to interface with both TEM and SEM microscopes. Silicon nitride chips were UV/O_3 plasma-cleaned using ProCleaner™ for 30 minutes prior to use to ensure contaminant removal. The gel-loaded liquid cell was formed by sandwiching two SiN coated silicon chips with a 50 × 200 μm electron transparent 50 nm thick SiN opening etched from the center, forming imaging window. In our experiments, one SiN window had a 500 nm SU-8 spacer, while the other had no spacer. The two chips with a gel-patterned SiN window membrane and a bare SiN chip were sealed to prevent evaporation of the liquid. In all experiments described in this work, gel-patterned window was assembled on to be at the top of the cell, while the bottom chip was loaded liquid- and particle-free. Following the cell assembly and vacuum check, the sealed holder was inserted into the microscope and allowed to equilibrate for ~15 minutes before imaging in the HAADF S/TEM mode

working at magnification range *M =40,000 x* — 56*,000 x*, unless noted otherwise, and using a beam current of 38 *pA* (spot size 9), with the beam blanked between image acquisitions. Similar experimental timeline was followed when imaging in the SEM with the FEI Teneo LoVac SEM equipped with STEM3 detector operating at 20 kV and imaging with a beam current 6.3 *pA* (spot size 4). Data analysis was performed with ES Vision (FEI) software (ES Vision version 4.12), DigitalMicrograph® (Gatan) software version 3.22.1461.0 and Origin® 2018.

2.9. Bulk gel specimen freezing, cryo-sectioning, and cryo-TEM imaging. Small volume of bulk gel sample was placed onto a bulls-eye stub, plunge-frozen at -190 ºC in liquefied ethane using a LEICA Plunge freezer (Mager Scientific Inc, Dexter, MI, USA.) and sectioned with a Reichert Ultracut S ultramicrotome with FCS cryo unit (Mager Scientific Inc., Dexter, MI). Sections were made using a Diatome cryo-diamond knife (35u-dry Electron Microscopy Sciences, Ft. Washington, PA, USA.) at 100 nm, collected onto 200 mesh carbon film copper grids, and placed into a grid transfer unit stored in liquid nitrogen until transferred to the TEM chamber. TEM samples were loaded into a liquid nitrogen cooled Gatan cold specimen holder (Model 626DH, Gatan Inc. Pleasanton, CA, USA.) and imaged using a JEOL JSM STEM operating at 200 kV (Japan Electron Optics Laboratories, LLC, USA, Peabody, MA), working in a bright field TEM mode.

3. RESULTS AND DISCUSSION

Aqueous F127 Poloxamer solutions with gold nanoparticles were used as a model system for *in situ* imaging of gel-based nanocomposites and individual nanoparticles in gels. In general, there are two ways to obtain polymer-nanoparticle composites: adding or mixing the nanoparticles into existing polymeric matrix, and synthesizing the nanoparticles within the polymeric matrix, the latter often referred to as an *in situ* method [50]. Accordingly, two systems were analyzed: the gel loaded with commercially available Au nanoparticles functionalized with mPEG-SH (ready type) and Au nanoparticles formed *in situ* by a reduction of $HAuCl_4$ in citrate-bearing F127 Poloxamer gel (prepared type). Ready Au nanoparticles suspended in water after PEG functionalization (in the absence of Poloxamer) were examined with conventional bright field TEM imaging as shown in **Figure 1 (a)**. **Figure 1 (b)** shows the nanoparticles formed within the gel, obtained after removing the gel matrix by an excessive washing with cold water. Formation of Au nanoparticles in citrate-bearing gels is discussed in the SI. From a group of ~100 nanoparticles, the size distribution was determined to be 5.1±1.0 nm for the ready type and 13.0±2.4 nm for the *in situ* gel-formed type. Supplementary information, **Figure S1**, shows UV/Vis absorbance spectra and hydrodynamic radius of the ready type nanoparticles before and after surface functionalization. Formation of the nanoparticles in the gel was determined by following the evolution of

the absorbance spectra of F127-citrate $HAuCl_4$ as a function of time, presented in Supplementary Information **Figure S2.**

Rheological data for aqueous F127 Poloxamer solutions are plotted in **Figure 2 (a, b)** for 30 ± 0.05 wt%, and 22.6 ± 0.05 wt%, respectively. G' and G" values are related to the storage modulus (stored deformation energy) and the loss modulus (dissipated energy), respectively. *Tan (δ)* represents the ratio of G" to G' and corresponds to a relative measure of the solid or liquid-like behavior of the material. For $tan(\delta)<1$, a solid-like behavior is observed, and so for these specific concentrations, critical gelation temperatures (CGT) are estimated to be 11 ºC for 30 ± 0.05 wt% and 20 ºC for 22.6 ± 0.05 wt% of F127 Poloxamer solutions. **Figure 2 (c)** shows a photograph of a vial containing 22.6 ± 0.05 wt% F127 Poloxamer solution loaded with Au-PEG nanoparticles composite at room temperature exhibiting gel-like behavior (the absence of flow). The rheological data for the citrate-bearing gel before and after formation of Au nanoparticles *in situ* are discussed in Supplementary Information **Figure S3.**

Cryo-TEM imaging of cryo-microtomed thin sections of gel-based nanocomposites is one of the conventional characterization methods prone to artifacts such as knife marks or occasional ice crystals [51]. A bright field cryo-TEM image of cryo-sectioned nanocomposite Poloxamer gel at 30 ± 0.05 wt% with 207 nM Au nanoparticles is shown in **Figure 3.** Here, three individual nanoparticles can be identified. Faint knife marks appear diagonally both on the left and on the right of the nanoparticles.

In this work, we utilized a fluid cell S/TEM imaging *in situ* to visualize nanoparticles in aqueous Poloxamer gels. Although Au nanoparticles have been used as a prototype to estimate the nanoscale resolution of FC-S/TEM as a function of water thickness [52], nanoparticles embedded in a gel matrix represent an extra challenge due to its nature. This poses difficulties for dispensing of adequately small highly-viscous specimen to preserve the membrane integrity and allow the cell to be assembled, and leads to additional scattering from polymeric carrier gel matrix itself. To overcome the first challenge, we used a previously devised process to deposit liquids directly onto a surface of choice with high lateral precision using a Nano eNabler™ molecular printer, as described elsewhere [53]. Using such an approach to sample deposition permitted deposition of extremely small amounts of liquid (attoliters to femtoliters) [54,55] and produced patterned specimen with a tunable thickness suitable for the subsequent imaging in a fluid cell. Patterson *et al.*[56] reported on alternative approach to dispensing picoliter-volumes of aqueous solutions onto SiN membranes.

We have expanded our method to be compatible with deposition of viscous liquids known to form gel upon temperature modulation. Specifically, we used a custom-built temperature-controlled stage to deposit polymeric nanocomposites at the highest temperature below the Critical Gelation Temperature (CGT) where the specimens behaved as a liquid. A representative video of nanocomposite deposition, in viscous liquid form, directly onto a 50 nm thick SiN membrane window, is presented in supplementary information **Video 1**. The stage housing the chips with the electron transparent SiN window membranes was maintained at a temperature 1-2 ºC below the CGT during the patterning process. Immediately following the deposition of viscous polymer specimen, the patterned windows were allowed to rest on cold stage to promote flattening of the freshly deposited droplets on the SiN membrane, while monitoring the appropriate humidity levels to ensure the specimen did not dry. A diagram of the Surface Patterning Tool used to deposit liquid on the window is presented in **Figure 4 (a)**. In **Figure 4 (b)**, a patterned SiN window is shown next to a custom-built temperature-controlled stage used with a top insulating stage to mitigate condensation on the patterned substrates, equipped with the basic temperature readout. The SiN chip on the top stage is marked with the red square. Inset shows optical images acquired from the freshly deposited pattern and after 15 minutes of rest on a cold stage in a controlled humidity atmosphere. Allowing the patterned substrate to rest on a cold stage results in a slight spreading of the deposited micro-droplets. This approach permitted reducing the overall thickness of the specimen layer and ensured its uniformity. Upon the completion of the patterning, the substrate chips were brought to room temperature to allow for the patterned micro-droplet volumes to form gel, while being kept in a high humidity chamber to prevent drying. Since the formed gel did not flow, the pattern deposited on a window stabilized and did not spread further. Once the micro-droplets were brought to room temperature, their shape and height remained unchanged for the duration of specimen handling and fluid cell assembly, leading to localization of nanoparticles to gel spots - nanoparticles cannot escape their boundaries. Indeed, no nanoparticles were observed outside of the patterned droplets. For this reason, during S/TEM imaging with the fluid cell *in situ*, the thickness of the nanocomposite was not directly related to the final distance in between the SiN membranes. **Figure 4 (c-d)** shows a photograph and a diagram of the fluid cell assembly on Hummingbird Scientific liquid flow holder, respectively.

For practical applications, maintaining stable nanoparticle dispersion in the gel and mitigating the issues associated with physical and chemical stability of gel-based nanocomposites are of outmost importance for delivering a desired set of functionalities. For example, for drug delivery purposes, flocculation, chemical reaction or additional crystal growth of the nanoparticles in the polymeric matrix will affect the functionality of the nanocomposite. For the duration of patterning process at T < CGT, Au-

gel samples exhibited no evidence of nanoparticles sedimentation, and therefore, were presumed thermodynamically stable.

Having a stable gel nanocomposites micro-droplet pattern deposited on SiN window membranes, we now had a direct way of determining thickness of gel droplets with optical profilometry utilizing 3D confocal and interferometry (PSI, VSI) techniques in the same single sensor head. This non-contact technique allowed the acquisition of 3D microscopy imaging as well as reliable thickness measurements of the gel deposited on the surface of SiN windows, while preserving the integrity of the sample. Combining this approach with Sensofar's high NA objectives (0.95), vertical resolution was reduced to below 1 nm with the lateral resolution of 0.1 μm [52]. **Figure 4 (e)** shows a confocal image of a SiN window membrane patterned with the Au-gel nanocomposite specimen, with a color bar representing height variation scale. **Figure 4 (f)** shows a surface height profile measured along the line, drawn as a visual guide, in **Figure 4 (e)**. We were able to determine a height difference between points 1-2-3 (a point beyond the left rim, top, and a point beyond the right rim of the first droplet) being approximately ~600 nm for a droplet with ~13 μm in diameter, which corresponds to a total volume of ~53 fL. Smaller patterned droplet with a diameter of ~5 μm, shown on the far right of the line, exhibited thickness variation reaching as high as ~400 nm between the points 4-5 (a point inside the droplet, and a top point), corresponding to a volume of ~5 fL. On average, the height-to-diameter ratio of the printed gel spots, was determined to be ~1:20 for larger droplets and ~1:12 for smaller droplets, indicative of more regular spreading and less height variations for larger droplets. The subsequent fluid cell assembly and imaging, carried out at room temperature, represented direct visualization of nanoparticles dispersed in femtoliter-range volumes of gel with a thickness up to 600 nm. The outstanding precision of patterning such small volumes of viscous materials is rarely achievable with available deposition methods.

Use of S/TEM imaging with the fluid cell permitted visualization of gel-based nanocomposites *in situ*. Such an approach allowed characterization of Au nanoparticles dispersed in both gel nanocomposites with sufficient resolution, despite the presence of thick polymeric matrix. When working in HAADF S/TEM mode, the contrast of the image is mass-thickness related, with the signal intensity increasing monotonically with atomic number Z and the thickness of the sample. In our experiments, cooling the substrate after micro-droplet patterning permitted spreadability of the deposited volume, yielding somewhat flattened droplets. At the center of a patterned spot, height variations in the nanocomposite are small compared with the average thickness of the sample (for example, point 2 in **Figure 4 (e)**). Assuming a relatively constant thickness, HAADF-STEM intensity will be then dominated by Z-contrast ($I \sim Z^{1.7\text{-}2}$) [57]. In our study, gold nanoparticles distributed in gel produced strong scattering signal associated with their higher atomic number compared to the surrounding gel matrix comprised of water and organic

block copolymer. **Figure 5** shows examples of two different types of Au nanoparticles dispersed in polymeric gels imaged with HAADF S/TEM using a fluid cell *in situ*. Despite the presence of thick gel matrix, Au nanoparticles can be easily identified in both cases. **Figure 5 (a)** shows FC-S/TEM image of F127 Poloxamer gel 22.6 ± 0.05 wt% loaded with PEG-functionalized ready-type Au nanoparticles (5 nm). **Figure 5 (b)** presents results for Poloxamer-Au nanocomposite with nanoparticles (~13 nm) formed after addition of $HAuCl_4$ to the citrate-bearing Poloxamer gel. It is worth noting, that under the imaging conditions used in this work, we did not observe signs of damage associated with the loss of hydration exhibited by the specimen (i.e., bubble formation, evolution of gas from the gel, and/or crystallization of polymer). The dose delivered to the specimen while imaging can be calculated as $^{It}/_{eA}$ [58]. With $I = 38\ pA$ and frame time $t = 10.1\ s$, the two gel-based nanocomposites were exposed to 6.43 and 3.21$e^{-}/$ Å^2 for the ready-type and prepared-in-gel-type, respectively. Every effort was made to avoid the electron beam damage to the specimen and carry out imaging of Au nanoparticles dispersed in gel media in an unaltered state. Details regarding the threshold dose at which the nanocomposite becomes affected by the electron beam, are described in the Supplementary Materials and presented in **Figure S4**. *In-situ* EM-imaging of Au-gel nanocomposite yielded a series of 2D projections of three-dimensional nanoparticle arrangement in gel. Since it is unlikely for all nanoparticles dispersed in the gel matrix to be residing at the same depth, they are not at the same focal plane, as manifested by a slight defocus of some of them, denoted by arrows in **Figure 5 (a, b)**. We observed no particular order or specific arrangement of nanoparticles in our experiments, likely due their low concentration in gel-based nanocomposites. From a group of N =100 nanoparticles, the nanoparticle size distribution obtained with the fluid cell *in situ*, was determined to be 6.9 ± 1.5 nm for the ready-type (*M = 56,000 x*) and 13.4 ± 2.7 nm for the *in situ* gel-formed type (*M = 56,000 x*).

When comparing this dataset to the size distribution obtained for the nanoparticles imaged in the absence of gel (**Figure 1**), we noted an increase in mean diameter accompanied by a broadening of the size distribution for the ready-type nanoparticles (6.9 ± 1.5 nm *vs*. 5.1 ±1.0 nm), whereas that of nanoparticles formed *in situ* was much less affected (13.4 ± 2.7 nm *vs*. 13.0 ± 2.4 nm). The measurement was repeated with using the images acquired at higher magnifications and a larger group of nanoparticles, with a ready-type gel: from a group of N = 225 nanoparticles, the nanoparticle size distribution obtained with the fluid cell *in situ*, was determined to be 6.8 ± 1.3 nm (*M = 79,000 x, M = 110,000 x*). Although working under low-dose conditions contributed to the increase in the measured diameter and slight broadening of the size distribution, we attribute the main difference to the fact that images were acquired from nanoparticles dispersed in gel, resulting in them not being stationary, their position affected by thermal fluctuations, and smaller nanoparticles are more susceptible to displacement. Hydration or

"swelling" of smaller nanoparticle is more pronounced due to the presence of the ligand on nanoparticle surface, since ready-type nanoparticles are functionalized with PEG prior to loading to gel, and coupled with mobility of PEG-functionalized nanoparticles in gel, this presents additional difficulties in accurate measurement of their size. Larger nanoparticles, formed *in situ* and lacking the PEG ligand, are less susceptible to thermal fluctuations. Indeed, when images are acquired with the dry nanoparticles that are no longer hydrated, these details are lost.

The intensity of the signal produced by a single nanoparticle in a thick polymeric matrix is limited to the resolution of the instrument taking into account background noise. If we consider a group of nanoparticles in nearly the same focal plane, we can estimate the Signal-to-Noise-ratio (SNR) as [59],

$$SNR = \frac{N_S - N_B}{\sigma_B}$$

where N_B and σ_B represent the mean value of the noise in the background and their standard deviation, respectively. Both values can be obtained from a lateral line scan of a nanoparticle in a perpendicular direction with respect to the propagation of the electron beam. N_S is associated with a higher scattering signal from the nanoparticle and it can be fitted as the maximum of a Gaussian distribution around the pixels forming the nanoparticle. The noise can be interpreted as the mean value of the background containing the polymeric matrix. Assuming a homogenous noise signal from the scattering gel background, an example of a typical nanoparticle line scan is shown in **Figure 6 (a)** for the 6.8 nm (~5 nm, dry) ready-type Au-PEG nanoparticles loaded into F127 Poloxamer 22.6 ± 0.05 wt% gel, as well for ~13 nm nanoparticles formed *in situ* in citrate-bearing Poloxamer 22.7 ± 0.05 wt% gel after reduction of $HAuCl_4$ *in situ* in **Figure 6 (b)**. According to the Rose criterion [60,61], nanoparticles are assumed to be visible at SNR≥ 5, meaning the signal must be at least 5 times the surrounded background noise in order to be detected. Within this range, Rose criteria stablish a threshold to be confident in the signal that has been used to analyze EM images [59,62]. Under the same conditions, larger nanoparticles of ~13 nm have an average SNR of 15.7 ± 2.2, while smaller nanoparticles of 6.9 nm in size have an average SNR of 8.2 ± 0.9 for a group of N=10 nanoparticles. The lower SNR determined for the ready-type nanoparticles is consistent with having smaller particles dispersed in gel (~6.9 nm ready-type) in comparison with larger nanoparticles (13.4 nm *in situ* type) due to a different number of atoms contributing to high-angle scattering electrons. The broadening of the size distribution for the ready-type nanoparticles in gel can also contribute to the lower SNR by decreasing the average scattering signal compared to the background noise.

Additional imaging experiments were conducted using the removable fluid cell tip compatible with the SEM equipped with STEM3 detector, as described in Supplementary Information **Figure S5**. Using the fluid cell S/TEM imaging, we were able to detect and visualize individual nanoparticles as small as 6.8 nm and obtain realistic information about their dispersion, size and lateral distribution in a thick (~ 600 nm) layer of gel, while preserving its hydrated state.

4. Conclusions

In conclusion, we presented a novel approach to imaging gel-based nanocomposites utilizing a fluid cell holder. We deposited femtoliter-range amounts of viscous polymeric-based nanocomposite solutions directly onto SiN window membranes, allowed them to form gel, and followed by the S/TEM imaging of gel samples using a fluid cell holder. We demonstrated that *in situ* S/TEM imaging with the fluid cell is suitable for the analysis of nanoparticle size distribution within the gel matrix, free of artifacts associated with the conventional electron microscopy imaging, by preserving the hydrated nature of the sample. An increase in the mean diameter of the PEG-functionalized nanoparticles compared to dry state (6.9 ± 1.5 nm *vs*. 5.1 ±1.0 nm) was attributed to nanoparticle motion induced by thermal fluctuation to the hydration of these nanoparticles, contributing to the difficulty in measuring size. Nanoparticles as small as 6.8 nm were imaged with sufficient resolution inside hundreds of nanometers thick gel, as supported by the signal-to-noise-ratio (SNR) analysis. Our approach to sample deposition, imaging and analysis can serve as complementary or even alternative to the bright-field cryo-TEM imaging of gel-based nanocomposites in a vitrified form. One of the possible pathways to retrieve 3D information from the 2D imaging of gel-based nanocomposites with the fluid cell could be adapting a tilt-pairs approach used in cryomicroscopy to the analysis of the spatial distribution of nanoparticles dispersed in gel in the fluid cell. This requires that gel-based nanocomposite contains high enough concentration of nanoparticles, the tilt angles in excess of ±45 degrees are achievable, and sufficiently large datasets are generated. At the moment, FEI S/TEM instruments with a 5.5 mm pole piece gap, operating with the first generation of commercially available fluid cell holders permit ±22.5° tilt. We envision, with development and implementation of high-tilt fluid holder design and additional fine-tuning of our methodology, these types of experiments will become possible in the near future, opening new opportunities in a 3D analysis and reconstruction of the spatial ordering of nanoparticles dispersed in block copolymer gels. This can be used as the much needed direct visualization information and obtaining new data complementary to small angle scattering techniques.

Declaration of conflict of interest: none.

Acknowledgments

This work was supported by the U.S. Department of Energy (DOE), Office of Science, Basic Energy Sciences, Materials Sciences and Engineering Division. The imaging with a removable fluid cell tip compatible with the SEM was supported by the U.S. Department of Energy (DOE), Office of Science, Basic Energy Research, Office of Biological and Environmental Research. The research was performed at the Ames Laboratory, which is operated for the U.S. Department of Energy by Iowa State University under Contract No. DE-AC02-07CH11358. All TEM-related work was performed using instruments in the Sensitive Instrument Facility in Ames Laboratory. The authors wish to thank Tracey Stewart (Roy J. Carter High Resolution Microscopy Facility) for assistance with the BF cryo-TEM imaging.

Supplementary Material

Supplementary material for this manuscript can be found at https://doi.org/10.25380/iastate.7455404

Research data for this article

The datasets generated and analyzed for this study can be found at https://doi.org/10.25380/iastate.7455404.v2

Bibliography

1 Wan, Y. & Zhao. On the Controllable Soft-Templating Approach to Mesoporous Silicates. *Chemical Reviews* **107**, 2821-2860, doi:10.1021/cr068020s (2007).

2 Robbins, S. W. *et al.* Block copolymer self-assembly–directed synthesis of mesoporous gyroidal superconductors. *Science Advances* **2**, e1501119, doi:10.1126/sciadv.1501119 (2016).

3 Bockstaller, M. R., Mickiewicz, R. A. & Thomas, E. L. Block Copolymer Nanocomposites: Perspectives for Tailored Functional Materials. *Advanced Materials* **17**, 1331-1349, doi:10.1002/adma.200500167 (2005).

4 Song, D.-P. *et al.* Structural Diversity and Phase Behavior of Brush Block Copolymer Nanocomposites. *Macromolecules* **49**, 6480-6488, doi:10.1021/acs.macromol.6b01602 (2016).

5 Song, D.-P., Li, C., Li, W. & Watkins, J. J. Block Copolymer Nanocomposites with High Refractive Index Contrast for One-Step Photonics. *ACS Nano* **10**, 1216-1223, doi:10.1021/acsnano.5b06525 (2016).

6 Alexandridis, P. & Tsianou, M. Block copolymer-directed metal nanoparticle morphogenesis and organization. *European Polymer Journal* **47**, 569-583, doi:10.1016/j.eurpolymj.2010.10.021 (2011).

7 Förster, S. & Antonietti, M. Amphiphilic Block Copolymers in Structure-Controlled Nanomaterial Hybrids. *Advanced Materials* **10**, 195-217, doi:10.1002/(SICI)1521-4095(199802)10:3<195::AID-ADMA195>3.0.CO;2-V (1998).

8 Caseri, W. Nanocomposites of polymers and metals or semiconductors: Historical background and optical properties. *Macromolecular Rapid Communications* **21**, 705-722, doi:10.1002/1521-3927(20000701)21:11<705::AID-MARC705>3.0.CO;2-3 (2000).

9 Pitto-Barry, A. & Barry, N. P. E. Pluronic® block-copolymers in medicine: from chemical and biological versatility to rationalisation and clinical advances. *Polymer Chemistry* **5**, 3291-3297, doi:10.1039/C4PY00039K (2014).

10 Sehgal, R. R., Carvalho, E. & Banerjee, R. Mechanically Stiff, Zinc Cross-Linked Nanocomposite Scaffolds with Improved Osteostimulation and Antibacterial Properties. *ACS Applied Materials & Interfaces* **8**, 13735-13747, doi:10.1021/acsami.6b02740 (2016).

11 Chi, H.-Y., Hsu, H.-W., Tung, S.-H. & Liu, C.-L. Nonvolatile Organic Field-Effect Transistors Memory Devices Using Supramolecular Block Copolymer/Functional Small Molecule Nanocomposite Electret. *ACS Applied Materials & Interfaces* **7**, 5663-5673, doi:10.1021/acsami.5b00338 (2015).

12 Chiu, Y.-C., Shih, C.-C. & Chen, W.-C. Nonvolatile memories using the electrets of conjugated rod-coil block copolymer and its nanocomposite with single wall carbon nanotubes. *Journal of Materials Chemistry C* **3**, 551-558, doi:10.1039/C4TC02233E (2015).

13 Hanemann, T. & Szabó, D. V. Polymer-Nanoparticle Composites: From Synthesis to Modern Applications. *Materials* **3**, doi:10.3390/ma3063468 (2010).

14 Paul, D. R. & Robeson, L. M. Polymer nanotechnology: Nanocomposites. *Polymer* **49**, 3187-3204, doi:10.1016/j.polymer.2008.04.017 (2008).

15 Pozzo, D. C. & Walker, L. M. Macroscopic alignment of nanoparticle arrays in soft crystals of cubic and cylindrical polymer micelles. *The European Physical Journal E* **26**, 183-189, doi:10.1140/epje/i2007-10303-4 (2008).

16 Pozzo, D. C. & Walker, L. M. Small-angle neutron scattering of silica nanoparticles templated in PEO–PPO–PEO cubic crystals. *Colloids and Surfaces A: Physicochemical and Engineering Aspects* **294**, 117-129, doi:10.1016/j.colsurfa.2006.08.002 (2007).

17 Tamborini, E., Ghofraniha, N., Oberdisse, J., Cipelletti, L. & Ramos, L. Structure of Nanoparticles Embedded in Micellar Polycrystals. *Langmuir* **28**, 8562-8570, doi:10.1021/la301369z (2012).

18 Krekhova, M., Lang, T., Richter, R. & Schmalz, H. Thermoreversible Hydroferrogels with Tunable Mechanical Properties Utilizing Block Copolymer Mesophases As Template. *Langmuir* **26**, 19181-19190, doi:10.1021/la1040823 (2010).

19 Nambam, J. S. & Philip, J. Thermogelling Properties of Triblock Copolymers in the Presence of Hydrophilic Fe3O4 Nanoparticles and Surfactants. *Langmuir* **28**, 12044-12053, doi:10.1021/la302310y (2012).

20 Dao, M. M., Domach, M. M. & Walker, L. M. Impact of dispersed particles on the structure and shear alignment of block copolymer soft solids. *Journal of Rheology* **61**, 237-252, doi:10.1122/1.4974486 (2017).

21 Enlow, D. *et al.* Synthesis and characterization of self-assembled block copolymer templated calcium phosphate nanocomposite gels. *Journal of Materials Chemistry* **17**, 1570-1578, doi:10.1039/B613760A (2007).

22 Kanapathipillai, M. *et al.* Synthesis and Characterization of Ionic Block Copolymer Templated Calcium Phosphate Nanocomposites. *Chemistry of Materials* **20**, 5922-5932, doi:10.1021/cm703441n (2008).

23 Yusufoglu, Y. *et al.* Bioinspired synthesis of self-assembled calcium phosphate nanocomposites using block copolymer-peptide conjugates. *Journal of Materials Research* **23**, 3196-3212, doi:10.1557/JMR.2008.0388 (2008).

24 Yang, P., Zhao, D., Margolese, D. I., Chmelka, B. F. & Stucky, G. D. Generalized syntheses of large-pore mesoporous metal oxides with semicrystalline frameworks. *Nature* **396**, 152, doi:10.1038/24132 (1998).

25 Deng, Y. *et al.* Facile Synthesis of Hierarchically Porous Carbons from Dual Colloidal Crystal/Block Copolymer Template Approach. *Chemistry of Materials* **19**, 3271-3277, doi:10.1021/cm070600y (2007).

26 Xu, J., Wang, A., Wang, X., Su, D. & Zhang, T. Synthesis, characterization, and catalytic application of highly ordered mesoporous alumina-carbon nanocomposites. *Nano Research* **4**, 50-60, doi:10.1007/s12274-010-0038-0 (2011).

27 Dolan, J. A. *et al.* Optical Properties of Gyroid Structured Materials: From Photonic Crystals to Metamaterials. *Advanced Optical Materials* **3**, 12-32, doi:10.1002/adom.201400333 (2015).

28 Wanka, G., Hoffmann, H. & Ulbricht, W. Phase Diagrams and Aggregation Behavior of Poly(oxyethylene)-Poly(oxypropylene)-Poly(oxyethylene) Triblock Copolymers in Aqueous Solutions. *Macromolecules* **27**, 4145-4159, doi:10.1021/ma00093a016 (1994).

29 Knorowski, C. D., Anderson, J. A. & Travesset, A. Self-assembled ordered polymer nanocomposites directed by attractive particles. *The Journal of Chemical Physics* **128**, 164903, doi:10.1063/1.2907744 (2008).

30 Sknepnek, R., Anderson, J. A., Lamm, M. H., Schmalian, J. & Travesset, A. Nanoparticle Ordering via Functionalized Block Copolymers in Solution. *ACS Nano* **2**, 1259-1265, doi:10.1021/nn8001449 (2008).

31 Anderson, J. A., Sknepnek, R. & Travesset, A. Design of polymer nanocomposites in solution by polymer functionalization. *Physical Review E* **82**, 021803, doi:10.1103/PhysRevE.82.021803 (2010).

32 Mortensen, K. & Talmon, Y. Cryo-TEM and SANS Microstructural Study of Pluronic Polymer Solutions. *Macromolecules* **28**, 8829-8834, doi:10.1021/ma00130a016 (1995).

33 Dehvari, K., Lin, K.-S. & Hammouda, B. Small-angle neutron scattering studies of microenvironmental and structural changes of Pluronic micelles upon encapsulation of paclitaxel. *Journal of the Taiwan Institute of Chemical Engineers* **71**, 405-413, doi:10.1016/j.jtice.2016.11.027 (2017).

34 Prud'homme, R. K., Wu, G. & Schneider, D. K. Structure and Rheology Studies of Poly(oxyethylene−oxypropylene−oxyethylene) Aqueous Solution. *Langmuir* **12**, 4651-4659, doi:10.1021/la951506b (1996).

35 Lam, Y.-M., Grigorieff, N. & Goldbeck-Wood, G. Direct visualisation of micelles of Pluronic block copolymers in aqueous solution by cryo-TEM. *Physical Chemistry Chemical Physics* **1**, 3331-3334, doi:10.1039/A902369K (1999).

36 Dehvari, K., Lin, K.-S. & Wang, S. S. S. Small Angle X-Ray Scattering Characterization of Multifunctional Iron Oxide-Pluronic Nanocarriers: Effect of Temperature and Drug Encapsulation. *Nanoscience and Nanotechnology Letters* **8**, 667-670, doi:10.1166/nnl.2016.2210 (2016).

37 Rahme, K. *et al.* Pluronics-Stabilized Gold Nanoparticles: Investigation of the Structure of the Polymer–Particle Hybrid. *ChemPhysChem* **9**, 2230-2236, doi:doi:10.1002/cphc.200800358 (2008).

38 Williamson, M. J., Tromp, R. M., Vereecken, P. M., Hull, R. & Ross, F. M. Dynamic microscopy of nanoscale cluster growth at the solid–liquid interface. *Nature Materials* **2**, 532, doi:10.1038/nmat944 (2003).

39 Zheng, H. *et al.* Observation of Single Colloidal Platinum Nanocrystal Growth Trajectories. *Science* **324**, 1309-1312, doi:10.1126/science.1172104 %J Science (2009).

40 Evans, J. E. *et al.* Visualizing macromolecular complexes with in situ liquid scanning transmission electron microscopy. *Micron* **43**, 1085-1090, doi:10.1016/j.micron.2012.01.018 (2012).

41 Mirsaidov, Utkur M., Zheng, H., Casana, Y. & Matsudaira, P. Imaging Protein Structure in Water at 2.7 nm Resolution by Transmission Electron Microscopy. *Biophysical Journal* **102**, L15-L17, doi:10.1016/j.bpj.2012.01.009 (2012).

42 Peckys, Diana B., Mazur, P., Gould, Kathleen L. & de Jonge, N. Fully Hydrated Yeast Cells Imaged with Electron Microscopy. *Biophysical Journal* **100**, 2522-2529, doi:10.1016/j.bpj.2011.03.045 (2011).

43 Woehl, T. J. *et al.* Correlative Electron and Fluorescence Microscopy of Magnetotactic Bacteria in Liquid: Toward In Vivo Imaging. *Scientific Reports* **4**, 6854, doi:10.1038/srep06854 (2014).

44 Jiao, X., Roiban, L., Foray, G. & Masenelli-Varlot, K. Electron tomography on latex particles suspended in water using environmental scanning electron microscopy. *Micron* **117**, 60-67, doi:10.1016/j.micron.2018.11.007 (2019).

45 Dearnaley, W. J. *et al.* Liquid Cell Electron Tomography for Biomedical Applications. *Microscopy and Microanalysis* **24**, 268-269, doi:10.1017/S1431927618001836 (2018).

46 Park, J. *et al.* 3D structure of individual nanocrystals in solution by electron microscopy. *Science* **349**, 290, doi:10.1126/science.aab1343 (2015).

47 Evans, J. E. & Browning, N. D. Enabling direct nanoscale observations of biological reactions with dynamic TEM. *Microscopy (Oxford, England)* **62**, 147-156, doi:10.1093/jmicro/dfs081 (2013).

48 Parent, L. R. *et al.* Direct in Situ Observation of Nanoparticle Synthesis in a Liquid Crystal Surfactant Template. *ACS Nano* **6**, 3589-3596, doi:10.1021/nn300671g (2012).

49 Parent, L. R. *et al.* In Situ Observation of Directed Nanoparticle Aggregation During the Synthesis of Ordered Nanoporous Metal in Soft Templates. *Chemistry of Materials* **26**, 1426-1433, doi:10.1021/cm4035209 (2014).

50 Mehdizadeh Taheri, S., Fischer, S. & Förster, S. Routes to Nanoparticle-Polymer Superlattices. *Polymers* **3**, doi:10.3390/polym3020662 (2011).

51 Franken, L. E., Boekema, E. J. & Stuart, M. C. A. Transmission Electron Microscopy as a Tool for the Characterization of Soft Materials: Application and Interpretation. *Advance Science* **4**, 1600476, doi:doi:10.1002/advs.201600476 (2017).

52 Schuh, T. & de Jonge, N. Liquid scanning transmission electron microscopy: Nanoscale imaging in micrometers-thick liquids. *Comptes Rendus Physique* **15**, 214-223, doi:10.1016/j.crhy.2013.11.004 (2014).

53 Kashyap, S., Woehl, T. J., Liu, X., Mallapragada, S. K. & Prozorov, T. Nucleation of Iron Oxide Nanoparticles Mediated by Mms6 Protein in Situ. *ACS Nano* **8**, 9097-9106, doi:10.1021/nn502551y (2014).

54 Xua, J. *et al.* Microfabricated "Biomolecular Ink Cartridges"—Surface patterning tools (SPTs) for the printing of multiplexed biomolecular arrays. *Sensors Actuators B*, 1034–1041 (2006).

55 Xu, J. *et al.* Microfabricated Quill-Type Surface Patterning Tools for Creation of Biological Micro/Nano Arrrays. *Biomed. Microdevices* **6**, 117-123 (2004).

56 Patterson, J. P. *et al.* Picoliter Drop-On-Demand Dispensing for Multiplex Liquid Cell Transmission Electron Microscopy. *Microscopy and Microanalysis* **22**, 507-514, doi:10.1017/S1431927616000659 (2016).

57 Williams, D. B. & Carter, C. B. Transmission electron microscopy : a textbook for materials science. (2009).

58 Abellan, P. *et al.* Factors influencing quantitative liquid (scanning) transmission electron microscopy. *Chemical Communications* **50**, 4873-4880, doi:10.1039/C3CC48479C (2014).

59 Demers, H., Poirier-Demers, N., Drouin, D. & de Jonge, N. Simulating STEM Imaging of Nanoparticles in Micrometers-Thick Substrates. *Microscopy and microanalysis : the official journal of Microscopy Society of America, Microbeam Analysis Society, Microscopical Society of Canada* **16**, 795-804, doi:10.1017/S1431927610094080 (2010).

60 Rose, A. *Vision : human and electronic*. (Plenum Press, 1974).

61 Rose, A. The Sensitivity Performance of the Human Eye on an Absolute Scale*. *J. Opt. Soc. Am.* **38**, 196-208, doi:10.1364/JOSA.38.000196 (1948).

62 Welch, D. A., Faller, R., Evans, J. E. & Browning, N. D. Simulating Realistic Imaging Conditions For In-Situ Liquid Microscopy. *Ultramicroscopy* **135**, 10.1016/j.ultramic.2013.1005.1010, doi:10.1016/j.ultramic.2013.05.010 (2013).

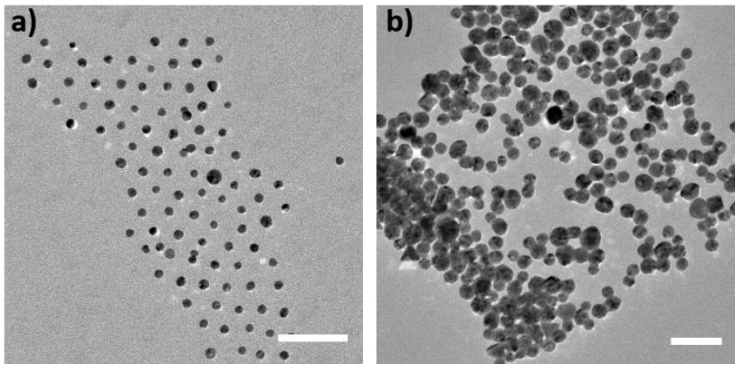

Figure 1. Bright field TEM images of nanoparticles used in this work. **(a)** Ready Au-PEG functionalized nanoparticles (NP) to be mixed with F127 Poloxamer gel, and **(b)** the nanoparticles extracted from the F127 Poloxamer citrate-bearing gel formed by the *in situ* reduction of $HAuCl_4$. Scale bar: 50 nm.

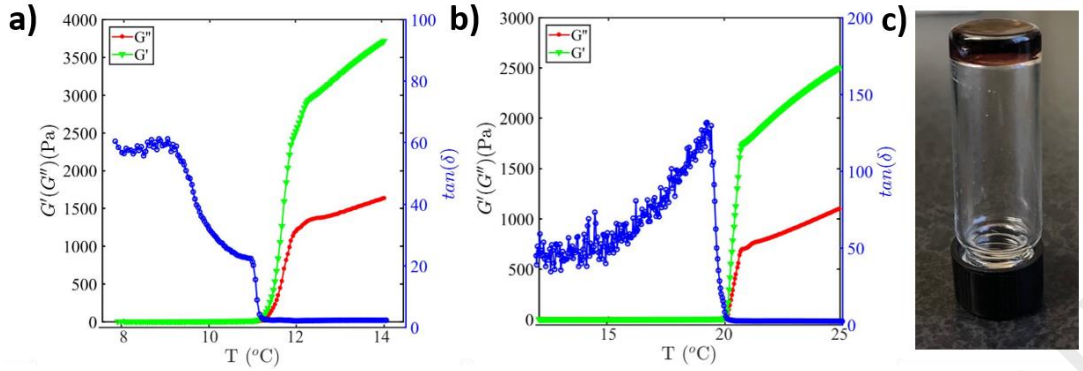

Figure 2. Rheological data for aqueous F127 Poloxamer solutions at working concentrations. **(a)** 30 ± 0.05 wt%, and **(b)** 22.6 ± 0.05 wt% used in this study. Increase of moduli G" (red) and G' (green) is consistent with temperature-induced increase of viscosity, with a sharp decrease in their ratio, *tan (δ)* (blue), signaling liquid-to-gel transition. **(c)** Photograph of a vial containing 22.6 ± 0.05 wt% F127 Poloxamer solution loaded with Au-PEG nanoparticles. Here, the absence of flow in the inverted vial at room temperature serves as a confirmation that the specimen behaves as a gel.

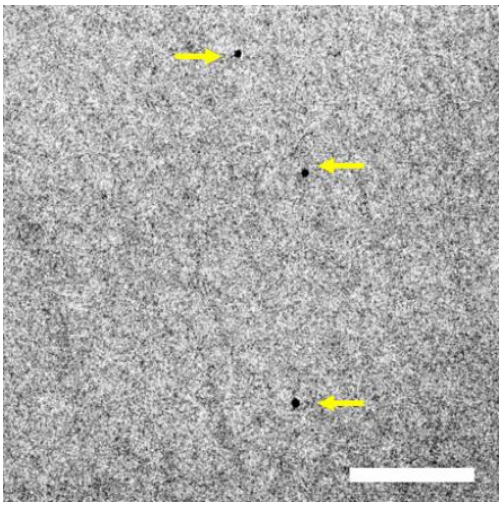

Figure 3. Bright field cryo-TEM image of the cryo-sectioned 30 ± 0.05 wt% F127 Poloxamer-based nanocomposite gel containing 5 nm 207 nM ready-type Au-PEG NPs. Nanoparticles are denoted with arrows. Scale bar: 100 nm.

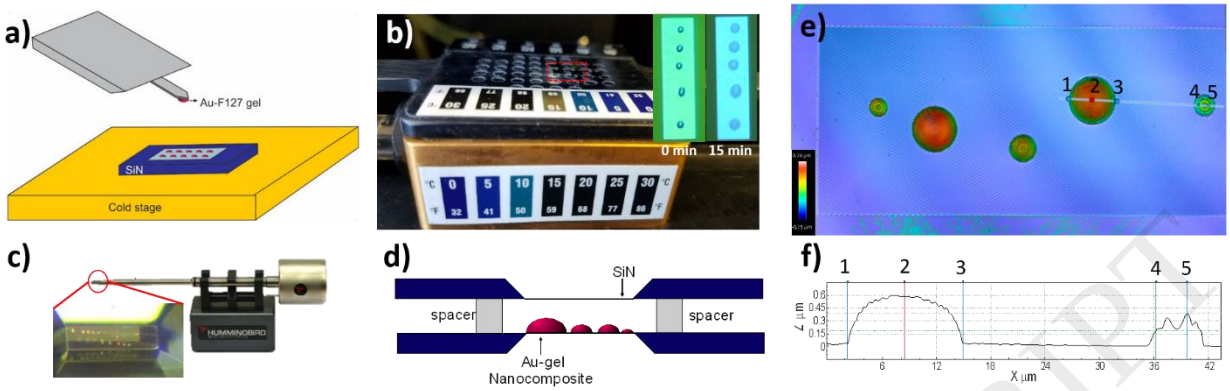

Figure 4. Deposition and cell assembly used for S/TEM imaging of Au-Poloxamer nanocomposite with the fluid cell holder *in situ*. **(a)** Diagram (not to scale) of the front-loaded Surface Patterning Tool (SPT) used to print micro-droplet of polymer to a SiN membrane for FC-S/TEM analysis. **(b)** Use of temperature-controlled stage permits deposition of thermoreversible polymeric samples in their liquid state, then allow for gels to form. Inset shows a patterned SiN membrane immediately following specimen deposition (0 min) and after 15 min of rest on a cold stage. **(c)** Photograph of the fluid cell assembly with an optical image of a sealed cell in which individual patterned droplets are observed. **(d)** An imaging schematics of a cell accommodating a patterned window. **(e)** Confocal image of a gel-patterned SiN window membrane with a color bar representing height variation; **(f)** Height profile measured across the micro-droplets patterned on the window with ~600 nm between the markers 1-3 and ~400 nm between the markers 4-5.

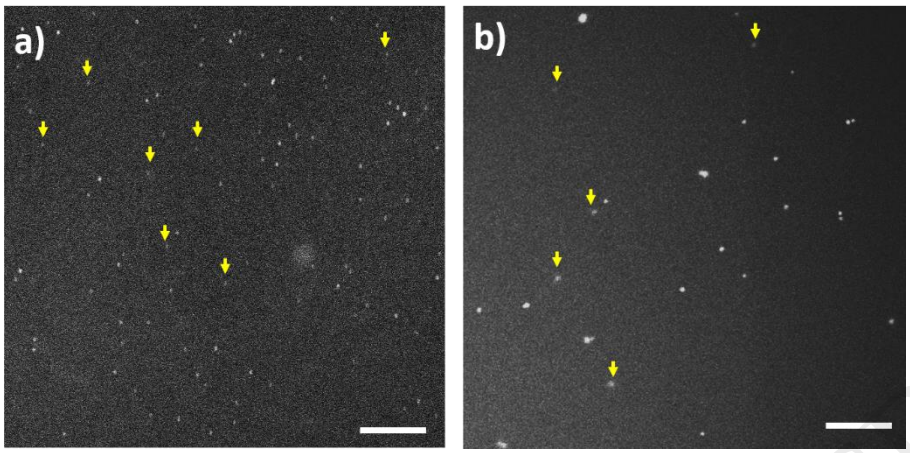

Figure 5. HAADF S/TEM imaging of aqueous Poloxamer-based gel nanocomposites with the fluid cell *in situ*. **(a)** 22.6 ± 0.05 wt % Au-F127 Poloxamer gel with 570 nM Au-PEG nanoparticles, *M = 56,000 x*. **(b)** 22.7 ± 0.05 wt % Au-F127 Poloxamer gel with Au nanoparticles formed *in situ* in the presence of sodium citrate, *M = 40,000 x*. Both images were digitally zoomed in and cropped to the same scale. Nanoparticles are clearly seen in a surrounding viscous gel matrix. Scale bar: 200 nm.

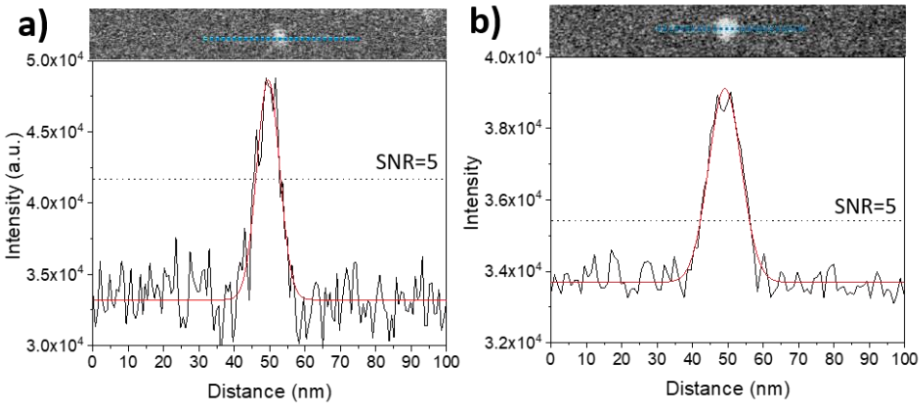

Figure 6. Intensity line scans of a random single particle dispersed in aqueous gel matrix. **(a)** ~6.8 nm ready-type Au-PEG functionalized NP loaded into 22.7 ± 0.05 wt% F127 Poloxamer gel, and **(b)** ~13 nm prepared-type Au NP synthesized in 22.7 ± 0.05 wt% F127 Poloxamer citrate-bearing gel *in situ*. The Rose criteria threshold of SNR=5 for establishing visibility of nanoparticles are shown in each graph.